Optical Materials 149 (2024) 115059

Contents lists available at ScienceDirect

Optical Materials

journal homepage: www.elsevier.com/locate/optmat

Research Article

# Sol-gel synthesis and property studies of $Cu_{0.4}Mg_{0.4}Co_{0.2}FeCrO_4$ spinel ferrite for optoelectronic, magnetic, and electrical applications

Mohamed Lamjed Bouazizi [a,*], Sobhi Hcini [b], Kamel Khirouni [c], Michel Boudard [d]

[a] Department of Mechanical Engineering, College of Engineering, Prince Sattam Bin Abdulaziz University, Alkharj 16273, Saudi Arabia
[b] Faculty of Science and Technology of Sidi Bouzid, University Campus Agricultural City, University of Kairouan, 9100 Sidi Bouzid, Tunisia
[c] Laboratory of Physics of Materials and Nanomaterials Applied to the Environment (LaPhyMNE), Faculty of Sciences of Gabès Cited Erriadh, University of Gabès, 6079 Gabès, Tunisia
[d] University of Grenoble Alpes, CNRS, Grenoble INP, LMGP, 38000 Grenoble, France

ARTICLE INFO

*Keywords:*
Spinel ferrites
Optoelectronic applications
Soft magnetic devices
Microwave absorption devices

ABSTRACT

This study investigated the properties of $Cu_{0.4}Mg_{0.4}Co_{0.2}FeCrO_4$ spinel ferrite synthesized using the sol-gel technique. The analysis covered thermal, morphological, structural, optical, magnetic, and electrical characteristics. The X-ray pattern analysis using Rietveld's refinement confirmed the well-formed cubic spinel structure of the sample. Optical properties were evaluated through absorbance measurements and the Tauc method, revealing a direct optical transition with low band-gab energy. The sample exhibited a significantly low Urbach energy, indicating minimal disorder and defects within its structure. Additionally, a study of other optical parameters such as refractive index, penetration depth, extinction coefficient, optical conductivity, and optical dielectric constants was comprehensively studied. These optical parameters provided valuable insights into the potential optoelectronic applications of the synthesized sample. The electrical conductivity study revealed that the sample exhibited semiconductor behavior, conforming to the CBH conduction model. Moreover, the $Cu_{0.4}Mg_{0.4}Co_{0.2}FeCrO_4$ spinel ferrite showcased low coercive field and high electrical resistivity, making it a promising candidate for soft magnetic devices and microwave absorption devices.

## 1. Introduction

In recent years, extensive research was conducted on nanomaterials due to their small size and unique properties [1–3]. These materials have found diverse applications in domains such as electronics, optoelectronics, fuel cells, solar cells, and the biomedical sector [4]. Researchers have synthesized and extensively studied a wide range of nanomaterial families to explore their potential for both fundamental scientific research and technological applications. Notably, several nanomaterials have gained attention in recent years, including spinel oxides [5–8], nanocomposites [9,10], and perovskite materials [11–13]. Among them, ferrite nanoparticles, specifically $MFe_2O_4$ (where M represents a divalent ion), have attracted significant interest due to their remarkable attributes. The $MFe_2O_4$ chemical formula can be written as $(M_{\delta}^{2+}Fe_{1-\delta}^{3+})_A[M_{1-\delta}^{2+}Fe_{1+\delta}^{3+}]_BO_4^{2-}$, where A and B denote the tetrahedral and octahedral sites, respectively. The parameter $\delta$ signifies the extent of inversion, indicating the proportion of $Fe^{3+}$ ions occupying the A sites [14]. Ferrite samples have gained recent interest due to their extensive applications in various technological and industrial fields. These materials demonstrate desirable traits like chemical stability, cost-effectiveness, minimal dielectric and magnetic losses, high electrical resistivity, and high magnetic permeability [15–17]. As a result, $MFe_2O_4$ materials have found utility in various fields such as magnetic, electrical, and optoelectronic applications [18–21].

The sol-gel synthesis technique [22–24] is commonly employed for the fabrication of pure spinel ferrites. This technique provides numerous benefits, including homogeneous particle sizes, lower processing temperatures, precise control over chemical compositions, reduced annealing times, and improved material purity [25,26]. Furthermore, studies have demonstrated that by adjusting sol-gel parameters such as sintering temperature, pH solution, and sintering time, it is possible to effectively manipulate spinel ferrites' properties [27–29].

Cu–Mg spinel ferrites, known as $Cu_{1-x}Mg_xFe_2O_4$, have attracted considerable interest as soft magnetic materials due to their impressive magnetic properties, exceptional thermal stability, and chemical stability [30]. These materials have found use in various fields such as gas

* Corresponding author.
*E-mail address:* my.bouazizi@psau.edu.sa (M. Lamjed Bouazizi).

https://doi.org/10.1016/j.optmat.2024.115059
Received 13 December 2023; Received in revised form 22 January 2024; Accepted 7 February 2024
Available online 19 February 2024

sensing, adsorption, photocatalysis, and electronic components [31,32]. Both undoped and substituted forms of $Cu_{1-x}Mg_xFe_2O_4$ have been utilized in high-frequency applications within the telecommunications industry [33]. Due to their elevated resistivity and minimal eddy current losses, $Cu_{1-x}Mg_xFe_2O_4$ spinel ferrites are well-suited for a range of applications such as high-quality filters, transformer cores, radiofrequency circuits, operational devices, and read/write heads for high-speed digital tape [34,35]. However, investigations into Cu–Mg ferrites' optical properties have revealed relatively high bandgap energies [34]. As a result, these ferrites have limited photon absorption in the ultraviolet spectrum, making them unsuitable for various practical optoelectronic applications [36,37]. To address this limitation, it becomes crucial to reduce the bandgap energies of these ferrites, enabling them to absorb a broader range of light energy, including the sunlight spectrum [38,39].

This study aimed to enhance the performance of $Cu_{1-x}Mg_xFe_2O_4$ ferrites in various technological applications, such as optoelectronic, magnetic, and electrical devices. By focusing on the substitution of Co and Cr ions in Cu–Mg ferrites, we prepared spinel ferrite with a composition of $Cu_{0.4}Mg_{0.4}Co_{0.2}FeCrO_4$ using the sol-gel route. We conducted a comprehensive analysis of its thermal, morphological, structural, optical, magnetic, and electrical properties. The substitution of Co and Cr ions in Cu–Mg spinel ferrites has the potential to modify their average B-site radius and crystal geometry, thereby altering their physical properties. Previous studies have shown that the introduction of both $Co^{2+}$ and $Cr^{3+}$ creates energy levels within the band gap, resulting in a decrease in the band-gap energy, which is advantageous for optoelectronic devices [40,41]. Additionally, the substitution of $Co^{2+}$ and $Cr^{3+}$ ions has been found to reduce dielectric loss and increase the electrical resistivity of spinel ferrites, making them suitable for electrical applications, including high-frequency and microwave absorption devices [42,43]. In our investigation, we identified several advantages associated with the synthesized $Cu_{0.4}Mg_{0.4}Co_{0.2}FeCrO_4$ ferrite, including low Urbach and band gap energies, a low coercive field, and high electrical resistivity. Our findings demonstrate that the as-prepared $Cu_{0.4}Mg_{0.4}Co_{0.2}FeCrO_4$ ferrite exhibits a reduced band gap, coercive field, and activation energy compared to some $Cu_{1-x}Mg_xFe_2O_4$ compositions reported in previous studies, supporting its potential for improved performance in technological applications [34,35,44,45].

## 2. Synthesis and characterizations

The synthesis of $Cu_{0.4}Mg_{0.4}Co_{0.2}FeCrO_4$ spinel ferrite was carried out using the sol-gel method. Initially, high-purity nitrates [$Cu(NO_3)_2{\cdot}6H_2O$, $Mg(NO_3)_2{\cdot}6H_2O$, $Co(NO_3)_2{\cdot}6H_2O$, $Fe(NO_3)_3{\cdot}9H_2O$ and $Cr(NO_3)_3{\cdot}9H_2O$] with a purity above 99% were dissolved in deionized water and stirred at 90 °C. Once the nitrates were completely dissolved, precise amounts of citric acid ($C_6H_8O_7$) were added as a complexing agent for the metal ions. The pH solution was adjusted to 7 using ammonia solution. Subsequently, ethylene glycol ($HO(CH_2)_3OH$) was introduced as a polymerization agent, resulting in a viscous solution or gel. The gel precursors were then heated, leading to brown powder formation. The annealing process involved multiple cycles of grinding, pelleting, and sintering within a temperature range of 600 °C–1000 °C to achieve grain crystallization. This was done to obtain a single-phase product with well-defined crystallization. In this study, all characterizations were performed on $Cu_{0.4}Mg_{0.4}Co_{0.2}FeCrO_4$ spinel ferrite sintered at 1000 °C.

The sample properties were investigated through multiple analyses. Thermal behavior was examined with a thermogravimetric analyzer (TGA). The XRD pattern was generated in an angular range of 10°–80° using a Panalytical X'Pert Pro system with Cu-$K_\alpha$ radiation. The sample's morphology was observed using scanning electron microscopy (SEM: JSM-6380 LA). The infrared spectrum was captured in the wavenumber range of 400–1000 $cm^{-1}$ using an FTIR-8400S spectrometer. Optical properties were determined at wavelength ranging from 200 nm to 2400 nm with a UV-3101PC scanning spectrophotometer equipped with a dual-beam monochromator. Two light sources were employed: a Xenon lamp for UV–visible radiation and a Halogen lamp for infrared radiation. The hysteresis loop was measured in an applied field of ±10 kOe using a vibrating sample magnetometer (Lake Shore model 7400) at room temperature. Lastly, electrical conductivity was assessed by modifying the temperature (300 K $\leq T \leq$ 500 K) and frequency (40 Hz $\leq f \leq 10^6$ Hz) using an Agilent 4294 analyzer.

## 3. Results and discussion

### 3.1. Thermal analysis

Fig. 1 presents the thermal behavior of the $Cu_{0.4}Mg_{0.4}Co_{0.2}FeCrO_4$ spinel sample, showing weight loss ($W$%) versus temperature ($T$) and its differential thermal analysis (DTA). The weight loss process consists of two distinct stages. Initially, there is a reduction in weight of 1.5% below 400 °C on the $W(T)$ curve, with a peak observed at 355 °C on the $dW/dT$ curve. This decrease in mass within this temperature range suggests the release of residual gases and moisture [46,47]. During the second stage, a weight reduction takes place within the temperature range of 400–1000 °C, with a maximum loss of 10%. This is accompanied by the detection of an exothermic peak at 820 °C in the DTA curve, which signifies the formation of the spinel phase in the sample. Consequently, the calcination temperature can be optimized to any value above 820 °C.

### 3.2. Morphology and structure

Fig. 2a displays the SEM image of the $Cu_{0.4}Mg_{0.4}Co_{0.2}FeCrO_4$ ferrite, revealing a uniform distribution of cubic-shaped grains. The presence of minor voids can be attributed to the sample's inherent porosity. The sintering temperature influences the material's size distribution and agglomeration. In our case, the sample underwent sintering at a sufficiently high temperature of 1000 °C. This elevated sintering temperature facilitates the enhancement of crystallinity and homogenization of $Cu_{0.4}Mg_{0.4}Co_{0.2}FeCrO_4$ microstructure. Fig. 2b presents a statistical analysis of the grain size distribution. Using the Gaussian function, the histogram indicates an average grain size of 0.9 nm.

Fig. 3 shows the Rietveld refinement [48] of the XRD pattern for $Cu_{0.4}Mg_{0.4}Co_{0.2}FeCrO_4$ spinel ferrite, confirming the formation of a pure spinel phase in the sample. All peak positions were indexed using $Fd\bar{3}m$ space group (n° 227). The Rietveld refinement considers the cation distribution within the $Cu_{0.4}Mg_{0.4}Co_{0.2}FeCrO_4$ sample structure. This includes the arrangement of $Fe^{3+}$ ions at the A-site and $Cu^{2+}$, $Mg^{2+}$, $Co^{2+}$, $Cr^{3+}$ ions at the B-site as $(Fe_1^{3+})_A[Cu_{0.4}^{2+}Mg_{0.4}^{2+}Co_{0.2}^{2+}Cr_1^{3+}]_BO_4^{2-}$ [49–52]. This cation distribution results in an inversion degree of unity, indicating an inverse spinel structure for the sample. The calculated and observed patterns, as shown in Fig. 3, are in good agreement. Table 1

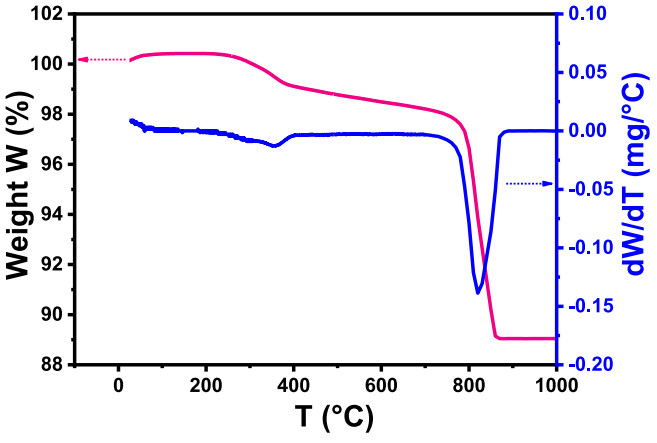


**Fig. 1.** TGA and DTA curves for $Cu_{0.4}Mg_{0.4}Co_{0.2}FeCrO_4$ spinel ferrite.

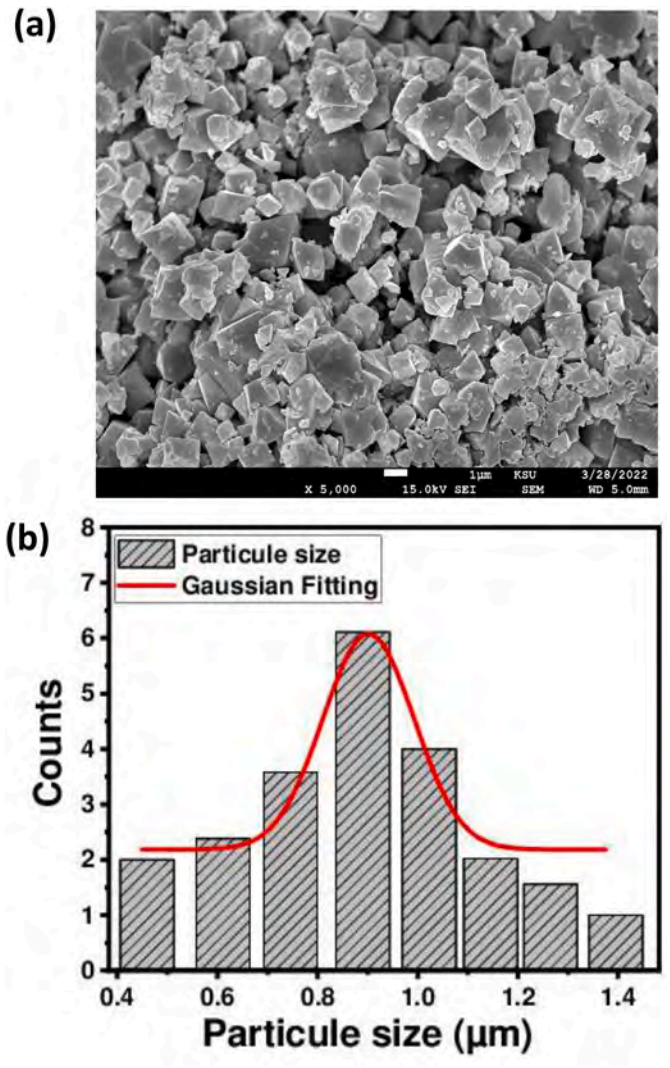


**Fig. 2.** (a) SEM image of $Cu_{0.4}Mg_{0.4}Co_{0.2}FeCrO_4$ spinel ferrite. (b) Grain size distribution.

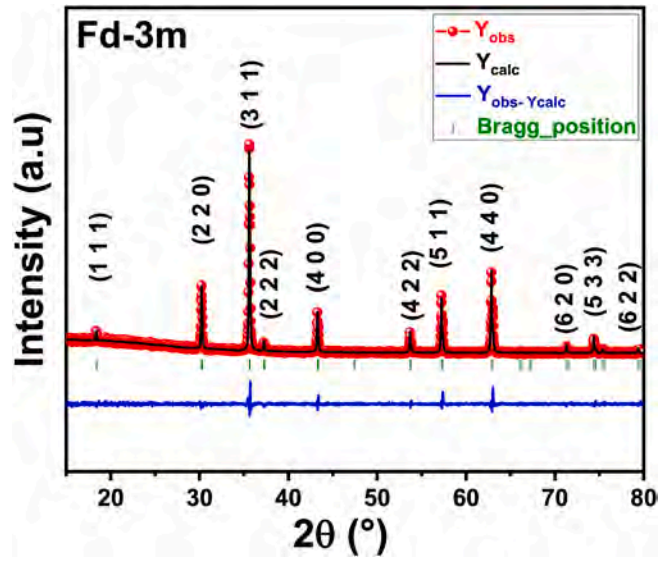


**Fig. 3.** XRD pattern of $Cu_{0.4}Mg_{0.4}Co_{0.2}FeCrO_4$ spinel ferrite with Rietveld analysis.

**Table 1**
Rietveld structural parameters for $Cu_{0.4}Mg_{0.4}Co_{0.2}FeCrO_4$ spinel ferrite. $B_{iso}$ represents the isotropic thermal agitation parameter. The specific definitions of structural parameters are defined in the corresponding text. Reliability R-factors: profile $R_p$, weighted profile $R_{wp}$, and structure $R_F$. $\chi^2$ represents the goodness of fit. The numbers provided in parentheses indicate the estimated standard deviations up to the last significant digit.

| *Sample* | | | $Cu_{0.4}Mg_{0.4}Co_{0.2}FeCrO_4$ |
|---|---|---|---|
| *Space group* | | | ***Fd$\bar{3}$m*** |
| ***Cell parameters*** | ***a (Å)*** | | 8.3568 (7) |
| | ***V (Å$^3$)*** | | 583.60 (8) |
| ***Atoms*** | ***Tetrahedral A site (Fe)*** | ***Atomic positions x = y = z*** | 1/8 |
| | | ***$B_{iso}$ (Å$^2$)*** | 0.3 (2) |
| | ***Octahedral B site (Cu/Mg/Co/Cr)*** | ***Atomic positions x = y = z*** | 1/2 |
| | | ***$B_{iso}$ (Å$^2$)*** | 1.2 (2) |
| | ***O*** | ***Atomic positions x = y = z*** | 0.2499 (8) |
| | | ***$B_{iso}$ (Å$^2$)*** | 0.2 (2) |
| ***Structural parameters*** | ***D (nm)*** | | 21 |
| | ***$d_{A\text{-}O}$ (Å)*** | | 1.808 (7) |
| | ***$d_{B\text{-}O}$ (Å)*** | | 2.090 (7) |
| | ***$\varphi_{(A\text{-}O\text{-}B)}$ (°)*** | | 125.3 (3) |
| | ***$\varphi_{(B-O-B)}$ (°)*** | | 90.0 (3) |
| ***Agreement factors*** | ***$R_p$ (%)*** | | 6.46 |
| | ***$R_{wp}$ (%)*** | | 8.64 |
| | ***$R_F$ (%)*** | | 4.24 |
| | ***$\chi^2$ (%)*** | | 1.38 |

presents the structural refinement results, including the typical oxygen coordinates for a spinel-type structure. The tetrahedral cation-oxygen bond length ($d_{A\text{-}O}$) is lower than the octahedral cation-oxygen bond length ($d_{B\text{-}O}$). Table 1 also displays the bond angles ($\varphi_{A\text{-}O\text{-}B}$ and $\varphi_{B\text{-}O\text{-}B}$) for the $Cu_{0.4}Mg_{0.4}Co_{0.2}FeCrO_4$ sample, where $\varphi_{A\text{-}O\text{-}B}$ represents A-O-B interactions and $\varphi_{B\text{-}O\text{-}B}$ represents B–O–B interactions [53]. The results indicate that $\varphi_{B\text{-}O\text{-}B}$ is lower than $\varphi_{A\text{-}O\text{-}B}$, suggesting a stronger exchange interaction between A-B sites than B–B sites. Using Scherer's formula [33], an average crystallite size ($D$) of approximately 21 nm is estimated. However, this value is lower than that derived from the SEM image, which is because each grain is characterized by multiple crystallite domains. Moreover, the $Cu_{0.4}Mg_{0.4}Co_{0.2}FeCrO_4$ compound exhibits a reduced lattice constant and cell volume compared to some $Cu_{1\text{-}x}Mg_xFe_2O_4$ compositions [54,55]. This is due to the decrease in the average B site radius caused by the substitution of $Co^{2+}$ and $Cr^{3+}$ ions within the $Cu_{1\text{-}x}Mg_xFe_2O_4$ ferrite system.

### 3.3. Optical properties

Fig. 4 illustrates the infrared spectroscopy analysis of $Cu_{0.4}Mg_{0.4}Co_{0.2}FeCrO_4$ spinel ferrite at room temperature. Here, typical absorption peaks associated with the intrinsic stretching vibrations of oxygen bands and metal ions situated at the (A) and [B] interstices of the spinel crystal can be observed [52]. As seen in Fig. 4, the spectrum displays two prominent peaks corresponding to tetrahedral and octahedral stretching vibrations. Tetrahedral vibration ($\nu_A$) occurs at a frequency of 625 cm$^{-1}$, while octahedral vibration ($\nu_B$) occurs at 503 cm$^{-1}$. Furthermore, through infrared spectroscopy analysis, it has been observed that the compound exhibits three distinct frequency bands at 891, 1040, and 1682 cm$^{-1}$. These bands correspond to the elongation and bending vibrations of the C–N═O, CC-C, and C═O groups, respectively [56]. Additionally, a broad absorption peak at 3445 cm$^{-1}$ indicates the presence of hydroxyl groups and absorbed water molecules within the compound [57].

Fig. 5a presents the UV-VIS-NIR absorbance ($A$) spectrum of $Cu_{0.4}Mg_{0.4}Co_{0.2}FeCrO_4$ spinel ferrite versus wavelength ($\lambda$). The

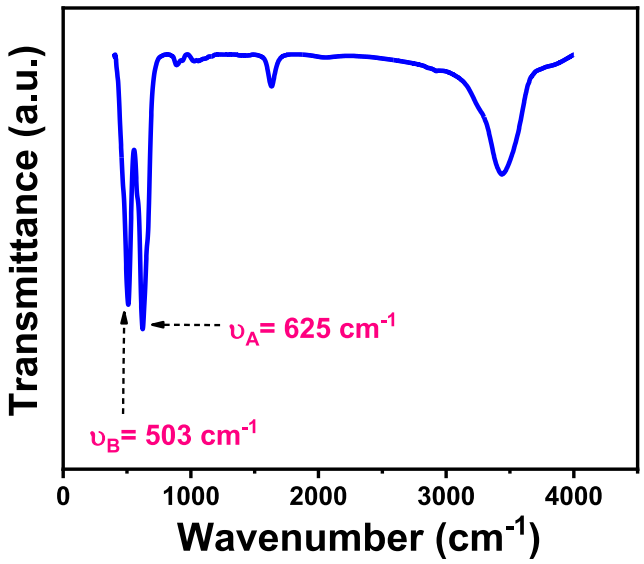


**Fig. 4.** FTIR spectrum for $Cu_{0.4}Mg_{0.4}Co_{0.2}FeCrO_4$ spinel ferrite.

reflectance spectrum $R(\lambda)$ is shown as an inset of the figure. The $A(\lambda)$ indicates an absorption band in the UV domain at a wavelength of $\lambda =$ 338 nm, suggesting that the sample exhibits desirable properties for absorbing UV light [58,59]. Furthermore, the prepared sample demonstrates wide absorption bands throughout the visible spectrum, ranging from 400 nm to 800 nm, indicating its potential suitability as a material for applications such as photo-catalysis and photovoltaic solar cells [60]. Additionally, the sample exhibits absorption bands within the near-infrared region of the spectrum, making it a good candidate for near-infrared optoelectronic devices [61]. Tauc's law [62] was used to estimate the band gap energy as follows:

$$\alpha h\nu = \beta\left(h\nu - E_g\right)^n \tag{1}$$

In this equation, $\alpha$ represents the absorption coefficient, $h\nu$ represents the photon energy, $\beta$ denotes the constant related to the disorder degree within the sample, and $E_g$ signifies the band-gap energy. The $n$ exponent value varies depending on the nature of the optical transition, where $n =$ 2 corresponds to a direct transition and $n = 1/2$ corresponds to an indirect transition. Direct optical transitions occur without a change in momentum and are typically observed in materials with small energy differences between the valence and conduction bands. Such transitions exhibit strong light absorption and emission, making them well-suited for applications in optoelectronics, lasers, and solar cells. On the other hand, indirect optical transitions occur in materials with significant energy differences between the valence and conduction bands, involving a change in momentum. Compared to direct transitions, indirect transitions exhibit less efficient light absorption and emission. However, materials with indirect bandgaps are commonly employed as host materials for phosphors in lighting technologies. The Beer-Lambert law [63] enables the calculation of the optical absorption coefficient ($\alpha$) by considering the sample's thickness ($d$) and absorbance ($A$):

$$\alpha = \frac{2.303 \times A}{d} \tag{2}$$

The $E_g$ energy can be determined by employing the Tauc formula, which is expressed as follows:

$$(\alpha h\nu)^{1/n} = \beta\left(h\nu - E_g\right) \tag{3}$$

In Fig. 5b, the $(\alpha h\nu)^{1/2}$ and $(\alpha h\nu)^2$ curves are presented, displaying their changes with respect to $h\nu$. Through linear extrapolation, the indirect band gap energy ($E_{gi}$) and direct band gap energy ($E_{gd}$) were determined

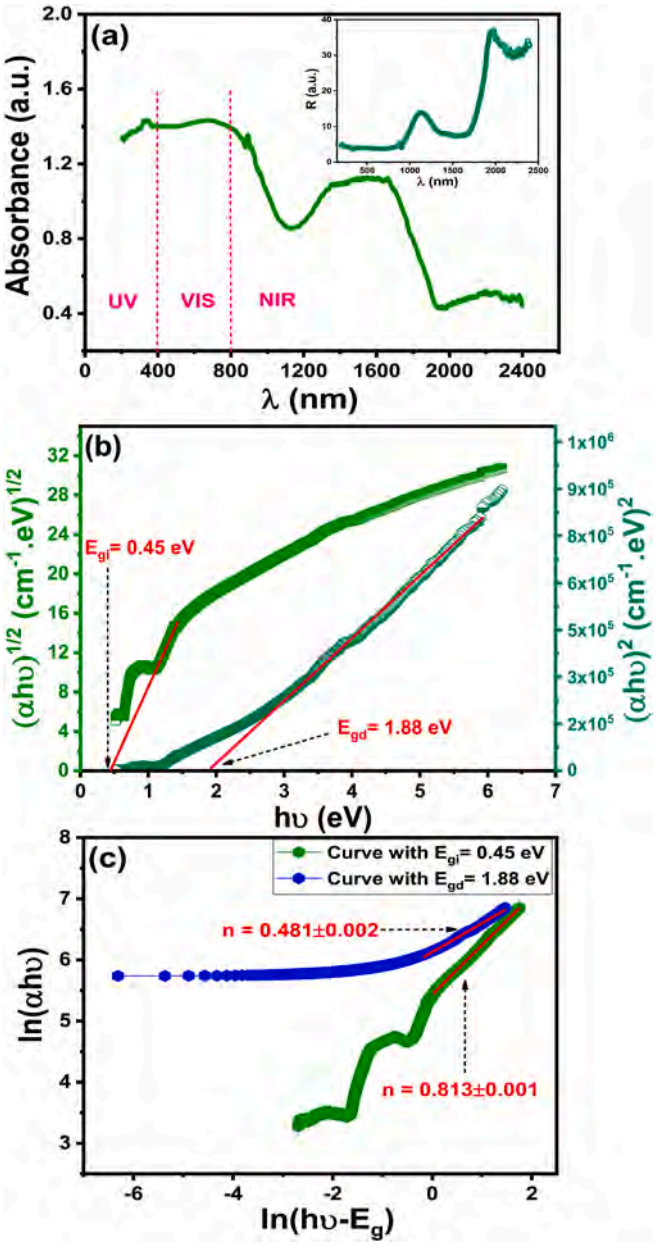


**Fig. 5.** (a) UV–VIS–NIR absorbance versus wavelength for $Cu_{0.4}Mg_{0.4}Co_{0.2}FeCrO_4$ spinel ferrite. The inset shows the reflectance spectrum $R(\lambda)$. (b) Plots of $(\alpha h\nu)^{1/2}$ and $(\alpha h\nu)^2$ versus $h\nu$. (c) Plots of ln $(\alpha h\nu)$ vs. ln $(h\nu\text{-}E_g)$.

as $E_{gi} = 0.45$ eV and $E_{gd} = 1.88$ eV. In order to further confirm the optical transition type observed in the sample, we generated plots of ln $(\alpha h\nu)$ versus ln $(h\nu\text{-}E_g)$ in Fig. 5c. These plots were constructed using the previously determined $E_{gi}$ and $E_{gd}$ energies. The fitting curve reveals $n$ value close to 0.5 ($n = 0.481 \pm 0.002$) for the direct optical transition, suggesting that the synthesized sample undergoes a direct optical transition, while the value for the indirect optical transition is noticeably lower than 2 ($n = 0.813 \pm 0.001$). Comparing the obtained band gap energy of $Cu_{0.4}Mg_{0.4}Co_{0.2}FeCrO_4$ spinel ferrite with other published values (see Table 2), we find a smaller $E_g$ energy of our sample than those reported for certain semiconductor materials [64–66]. Furthermore, the $E_g$ value for the as-prepared sample is lower than those of some $Cu_{1-x}Mg_xFe_2O_4$ compositions [34]. With the substitution of Co and Cr ions into $Cu_{1-x}Mg_xFe_2O_4$ compositions, the band gap energies of these materials are decreased, resulting in enhanced optical properties. Consequently, our sample exhibits potential as a viable material choice

**Table 2**
Band gap energy for $Cu_{0.4}Mg_{0.4}Co_{0.2}FeCrO_4$ spinel ferrite in comparison with those reported in previous works.

| Samples | Band gap energy (eV) | Reference |
|---|---|---|
| $TiO_2$ | 3.20 | [64] |
| ZnO | 3.37 | [65] |
| CuO | 3.85 | [66] |
| $CuFe_2O_4$ | 2.82 | [34] |
| $Cu_{0.8}Mg_{0.2}Fe_2O_4$ | 2.91 | [34] |
| $Cu_{0.6}Mg_{0.4}Fe_2O_4$ | 3.00 | [34] |
| $Cu_{0.2}Mg_{0.8}Fe_2O_4$ | 3.05 | [34] |
| $Cu_{0.8}Mg_{0.2}Fe_2O_4$ | 3.15 | [34] |
| $MgFe_2O_4$ | 3.31 | [34] |
| $Cu_{0.4}Mg_{0.4}Co_{0.2}FeCrO_4$ | 1.88 | This work |

for efficient visible light absorption. Furthermore, it is important to highlight that the $Cu_{0.4}Mg_{0.4}Co_{0.2}FeCrO_4$ sample exhibits an $E_g$ value that surpasses the energy threshold typically required for water splitting ($E_g > 1.23$ eV). Then, the synthesized sample holds potential for application as a photocatalytic material [67].

The Urbach energy (E*u*) provides insight into the disorder degree, defects, and impurities within a material, serving as a metric for the presence of localized states in the conduction band and extended transitions in the valence band [68,69]. In our compound, the E*u* value was determined as follows [70]:

$$\alpha = \alpha_0 \exp\left(\frac{h\nu}{E_u}\right) \tag{4}$$

where $\alpha_0$ and $h\nu$ represent a constant and the photon energy, respectively. By plotting ln($\alpha$) against ($h\nu$) in Fig. 6, the $E_u$ value for the $Cu_{0.4}Mg_{0.4}Co_{0.2}FeCrO_4$ sample was found to be 0.553 ± 0.003 eV. This value is considerably lower, suggesting that the sample exhibits a lower degree of disorder, fewer defects, and fewer localized states within its structure. The following relation [71] can be used to estimate the value of the steepness parameter S(T):

$$E_u = \frac{k_B T}{S(T)} \tag{5}$$

Here, kB represents the Boltzmann constant and $T$ denotes room temperature. The $S(T)$ parameter is a physical property associated with the band gap and represents the widening of the absorption edge caused by interactions between electrons or excitons with phonons [61]. In the case of the $Cu_{0.4}Mg_{0.4}Co_{0.2}FeCrO_4$ sample, the value of $S$ at room temperature was calculated to be 0.047. In addition, the electron-phonon interaction (Ee-ph) has an inverse relationship with the steepness parameter as follows [61]:

$$E_{e-ph} = \frac{2}{3S} \tag{6}$$

According to Eq. (6), the $E_{e\text{-}ph}$ value was estimated as 14.18 eV. The maximum wavelength ($\lambda_T$) of the incident radiation plays a crucial role in evaluating the appropriateness of a compound for optoelectronic devices, as it signifies the minimum wavelength needed for charge carrier expulsion. The value of $\lambda_T$ can be calculated from this equation [72]:

$$\left(\frac{\alpha}{\lambda}\right)^2 = C\left(\frac{1}{\lambda}\right) - \left(\frac{1}{\lambda_T}\right) \tag{7}$$

where $C$ is a constant. The threshold wavelength was estimated as 657 nm by plotting $\left(\frac{\alpha}{\lambda}\right)^2$ versus $\left(\frac{1}{\lambda}\right)$ in the inset of Fig. 6.

When a compound interacts with light, its absorption of particular radiation reduces the incoming photon flow. To comprehend the extent to which incident radiation can permeate the compound, we can use penetration depth or skin depth ($\delta$). The calculation of $\delta$ is based on the $\alpha(\lambda)$ curve and is expressed by the following relation [73]:

$$\delta = \frac{1}{\alpha(\lambda)} \tag{8}$$

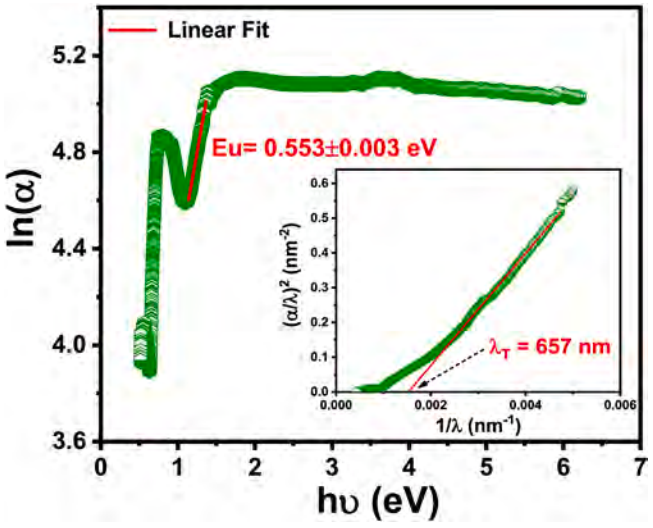


**Fig. 6.** Plot of ln(α) vs. $h\nu$ for $Cu_{0.4}Mg_{0.4}Co_{0.2}FeCrO_4$ spinel ferrite. The inset shows the curve of $(\alpha/\lambda)^2$ vs. $1/\lambda$.

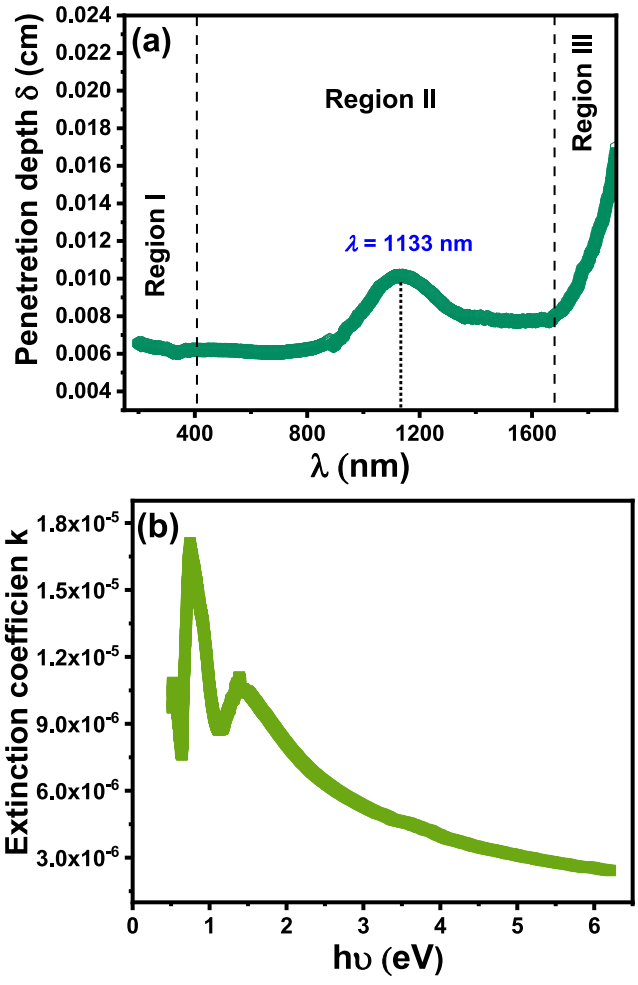


**Fig. 7.** (a) Penetration depth ($\delta$) vs. $\lambda$ for $Cu_{0.4}Mg_{0.4}Co_{0.2}FeCrO_4$ spinel ferrite. (b) Extinction coefficient ($k$) vs. $h\nu$.

In Fig. 7a, the $\delta(\lambda)$ curve for the $Cu_{0.4}Mg_{0.4}Co_{0.2}FeCrO_4$ sample exhibits three distinct regions. In the first region (region I) of the spectrum, our compound demonstrates complete UV radiation absorption, highlighting its potential as a highly efficient UV filter [72]. As we progress into the second region (region II), the $\delta(\lambda)$ increases, reaching its maximum at $\lambda = 1133$ nm. Subsequently, in the third region (region III), the $\delta(\lambda)$ values gradually increase up to 2400 nm. Furthermore, we can determine the extinction coefficient ($k$) as follows [74]:

$$k = \frac{\alpha\lambda}{4\pi} \tag{9}$$

In Fig. 7b, the plot of the extinction coefficient ($k$) curve for the $Cu_{0.4}Mg_{0.4}Co_{0.2}FeCrO_4$ sample versus photon energy ($h\upsilon$) is displayed. As the photon energy increases, there is a noticeable decrease in the $k$ coefficient, which can be attributed to the corresponding reduction in incident photon energy. Similar phenomena have been observed in other spinel materials as the wavelength increases [67,75].

The refractive index ($n$) holds significant importance in spectral dispersion applications as a fundamental parameter, and its expression in the visible range can be described as follows [76]:

$$n(\lambda) = \frac{1+R}{1-R} - \sqrt{\frac{4R}{(1-R)^2} - (k(\lambda))^2} \tag{10}$$

Where $R$ is the reflectance. Fig. 8a showcases the $n(\lambda)$ curve for the $Cu_{0.4}Mg_{0.4}Co_{0.2}FeCrO_4$ sample, revealing prominent absorption bands across the UV-VIS-NIR regions. These absorption bands in the $n(\lambda)$ curve prove the sample's exceptional quality and compactness. Additionally, the $n(\lambda)$ curve can be described using the Cauchy parameters, namely $n_0$, $n_1$, and $n_2$ as follows [75]:

$$n = n_0 + \frac{n_1}{\lambda^2} + \frac{n_2}{\lambda^4} \tag{11}$$

Cauchy analysis determines the refractive index for weak absorption materials. Fig. 8b presents the curve of $n$ versus $1/\lambda 2$, modeled through Eq. (11). From the fitting curve, we determined the Cauchy parameters for the sample as n0 = 1.48 ± 0.03, n1 = 1.39 ± 0.03 ($nm^2$), and n2 = 0.29 ± 0.01 ($nm^4$). Furthermore, in order to determine the energy of the effective single oscillator ($E_0$) and the dispersion energy ($E_d$), we utilized the Wemple-Didomenico relation [77], which is expressed as follows:

$$n^2 - 1 = \frac{E_0 E_d}{E_0^2 - (h\upsilon)^2} \tag{12}$$

Through the fitting of the linear segment in the curve of $\left(\frac{1}{n^2-1}\right)$ versus $(h\upsilon)^2$, displayed in Fig. 8c, we can determine the values of E*0* and E*d* for the $Cu_{0.4}Mg_{0.4}Co_{0.2}FeCrO_4$ sample. The slope of the linear portion corresponds to $\frac{1}{E_0 E_d}$, while the intercept with the vertical axis corresponds to $\frac{E_0}{E_d}$. Using the findings from this analysis, we determined the values of E*0* and E*d* to be 1.46 ± 0.01 eV and 1.60 ± 0.02 eV, respectively. Furthermore, by employing these values, we can estimate the dielectric constant (εop) at zero frequency and the static refractive index (n'0) from this equation:

$$\varepsilon_{op} = n_0^{'2} = 1 + \frac{E_d}{E_0} \tag{13}$$

Using this equation, we obtained values of 1.448 for εop and 2.095 for n'0. In particular, the calculated value for n'0 aligns closely with the value derived from the Cauchy fit. For the determination of the average oscillator strength (S0) and oscillator wavelength (λ0), we utilized the following relation [78]:

$$\frac{1}{n^2-1} = \frac{1}{S_0\lambda_0^2} - \frac{1}{S_0\lambda^2} \tag{14}$$

Fig. 8d displays the plotted curves of $\frac{1}{n^2-1}$ versus $\frac{1}{\lambda^2}$. By performing a linear fit to the curve, the values of $\lambda_0$ and $S_0$ were determined as 1178 nm and $0.84 \times 10^{-6}$ $m^{-2}$, respectively.

Fig. 9a displays the variation of the optical conductivity ($\sigma_{op}$) versus wavelength ($\lambda$) for $Cu_{0.4}Mg_{0.4}Co_{0.2}FeCrO_4$ sample according to the following relation [79]:

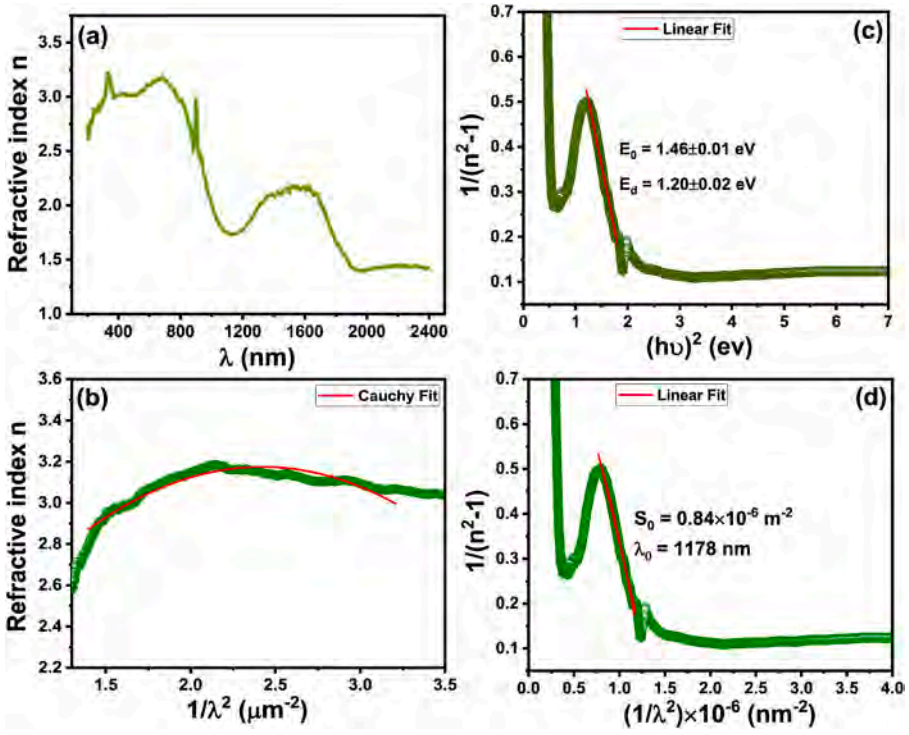


**Fig. 8.** (a) Refractive index $n$ vs. $\lambda$ for $Cu_{0.4}Mg_{0.4}Co_{0.2}FeCrO_4$ spinel ferrite. (b) Variation of $n(\lambda)$ curve with Cauchy fit. (c) Plot of $1/(n^2\text{-}1)$ vs. $(h\upsilon)^2$. (d) Plot of $1/(n^2\text{-}1)$ vs. $(1/\lambda)^2$.

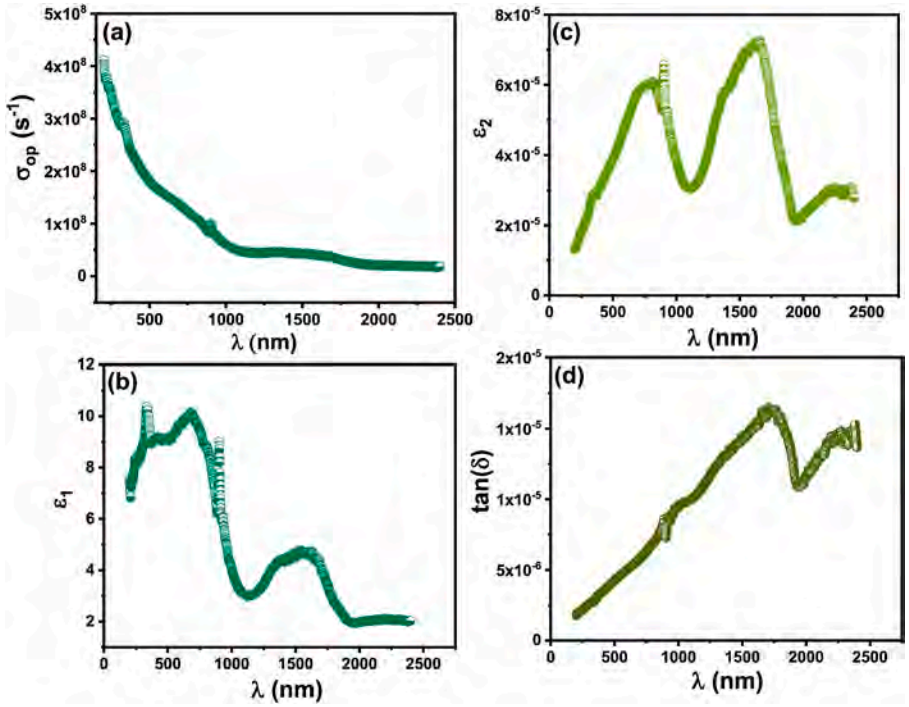


**Fig. 9.** (a) Optical conductivity vs. $\lambda$ for $Cu_{0.4}Mg_{0.4}Co_{0.2}FeCrO_4$ spinel ferrite. (b, c) Variations of real $\varepsilon_1(\lambda)$ and imaginary $\varepsilon_2(\lambda)$ parts of dielectric permittivity. (d) Variation of optical loss factor tan($\delta$).

$$\sigma_{opt} = \frac{\alpha(\lambda)n(\lambda)c}{4\pi k(\lambda)} \tag{15}$$

In this equation, $c$ represents the speed of light. The optical conductivity, which represents a material's ability to conduct light or electromagnetic radiation and describes its response to an oscillating electromagnetic field at optical frequencies [80], shows higher values at shorter wavelengths and lower values at longer wavelengths. The significant optical conductivity observed at shorter wavelengths can be attributed to the excitation of electrons by high-energy photons, explaining the sample's strong photo-response. Additionally, Additionally, optical dielectric permittivity is an indicator of a material's interaction efficiency with an electric or electromagnetic field. To calculate the complex dielectric permittivity, we utilized the following equation [81]:

$$\varepsilon(\lambda) = [n(\lambda) - ik(\lambda)]^2 = \varepsilon_1(\lambda) - i\varepsilon_2(\lambda) \tag{16}$$

In this equation, the real part ($\varepsilon_1$) and imaginary part ($\varepsilon_2$) of the optical dielectric permittivity can be represented by the following expressions:

$$\varepsilon_1(\lambda) = n^2(\lambda) - k^2(\lambda) \tag{17}$$

$$\varepsilon_2(\lambda) = 2n(\lambda)k(\lambda) \tag{18}$$

Fig. 9b, c displays the graphs of $\varepsilon_1(\lambda)$ and $\varepsilon_2(\lambda)$, revealing that the $\varepsilon_1(\lambda)$ plot follows a similar pattern as $n(\lambda)$ curve due to the presence of a low extinction coefficient $k(\lambda)$. Nevertheless, there is a slight rise in $\varepsilon_2(\lambda)$ as the wavelength increases, which aligns with similar observations made in other compounds [82]. On the other hand, the optical loss factor tan($\delta$) can be determined as follows [83]:

$$\tan(\delta) = \frac{\varepsilon_2(\lambda)}{\varepsilon_1(\lambda)} \tag{19}$$

Fig. 9d visually presents the relationship between the optical loss factor, tan($\delta$), and $\lambda$, indicating a clear upward trend where tan($\delta$) rises as the wavelength extends [84].

According to the following relations [85], the bulk loss energy ($V$-loss) and surface loss energy ($S$-loss) of the as prepared material was calculated in order to evaluate the contribution of the bulk and surface to the energy losses:

$$V - \text{loss}(\lambda) = \varepsilon_2^2 / \left(\varepsilon_1^2 - \varepsilon_2^2\right) \tag{20}$$

$$S - \text{loss}(\lambda) = \varepsilon_2^2 / \left((\varepsilon_1 + 1)^2 + \varepsilon_2^2\right)\big) \tag{21}$$

The distribution of volume and surface losses is depicted for the $Cu_{0.4}Mg_{0.4}Co_{0.2}FeCrO_4$ sample in Fig. 10. This figure shows that volume loss dominates over surface loss as observed by the changes in both $V$-loss($\lambda$) and $S$-loss($\lambda$) curves with wavelength, which aligns with similar findings in other samples [86,87].

### 3.4. Magnetic properties

The magnetic hysteresis curve of the $Cu_{0.4}Mg_{0.4}Co_{0.2}FeCrO_4$ ferrite at room temperature is presented in Fig. 11 at a magnetic field range of

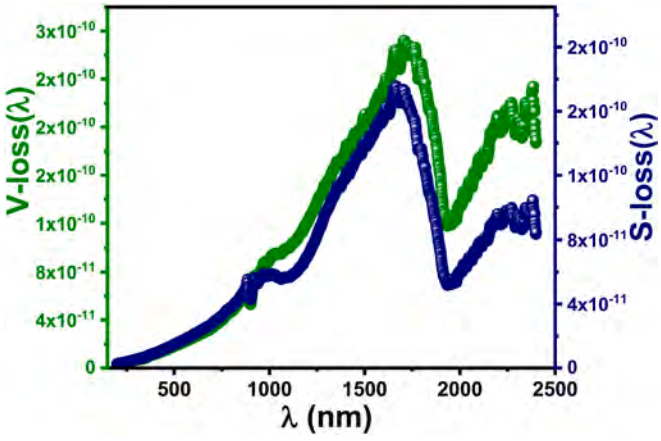


**Fig. 10.** Variation of volume loss ($V$-loss) and surface loss ($S$-loss) versus wavelength for $Cu_{0.4}Mg_{0.4}Co_{0.2}FeCrO_4$ spinel ferrite.

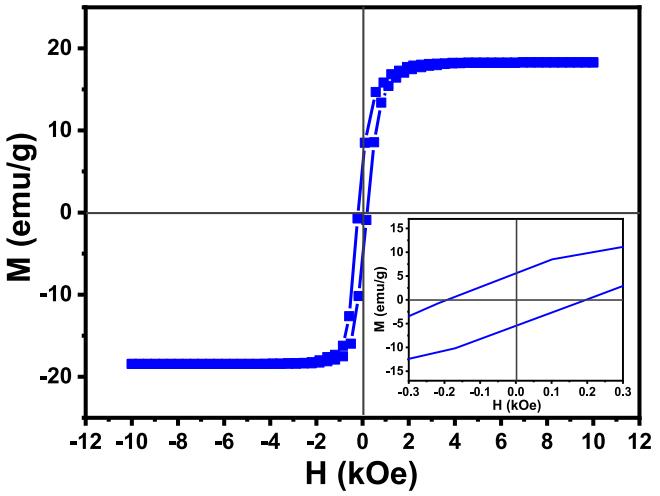


**Fig. 11.** Magnetic hysteresis loop for $Cu_{0.4}Mg_{0.4}Co_{0.2}FeCrO_4$ spinel ferrite at room temperature. The inset focuses on the curves near the origin, highlighting the remanence ($M_r$) and coercivity ($H_c$) values.

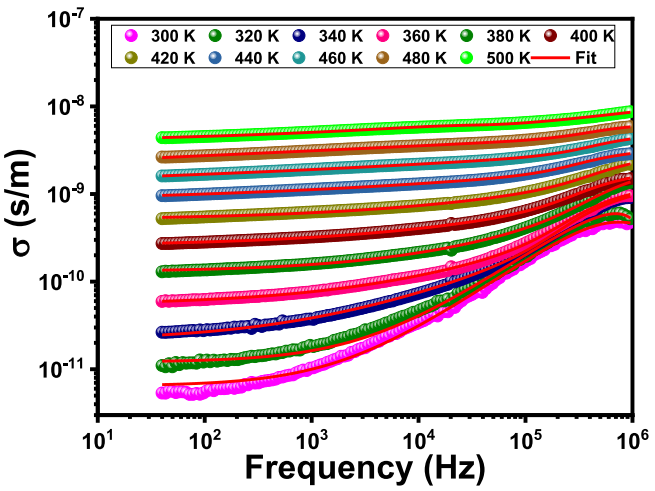


**Fig. 12.** $\sigma(T, f)$ curve for $Cu_{0.4}Mg_{0.4}Co_{0.2}FeCrO_4$ spinel ferrite. The red lines represent the fits using Eq. (24).

±10 kOe. It can be observed that magnetization exhibits a nonlinear increase at weak magnetic fields and reaches saturation at higher fields, indicating a ferromagnetic nature of the sample. The values of saturation magnetization ($M_s$), remanent magnetization ($M_r$), and coercivity ($H_c$) were estimated as 18.44 emu/g, 5.48 emu/g, and 195 Oe, respectively. Particularly, the sample demonstrates characteristics of a soft magnetic ferrite due to its relatively low coercivity ($H_c$). Consequently, $Cu_{0.4}Mg_{0.4}Co_{0.2}FeCrO_4$ ferrite holds potential for various magnetic applications, including transformers, recording-media applications, inductors, and electronic components [88–90]. According to Néel's theory [91], ferrite materials exhibit three types of interactions: B–B, A-A, and A-B sublattice interactions. The A-B super-exchange interaction surpasses the intrasublattice A-A and B–B interactions. The net magnetic moment can be estimated by calculating the vector sum of the magnetic moments at the A and B sublattices through the utilization of the following expression [92]:

$$n_B^{cal} = |M_B - M_A| \tag{22}$$

In this equation, $M_B$ and $M_A$ represent the magnetic moments of the B and A sublattices, respectively, measured in terms of Bohr magnetons ($\mu_B$). To determine $M_B$ and $M_A$, we can utilize the magnetic moments of $Mg^{2+}$ (0$\mu_B$), $Co^{2+}$ (3$\mu_B$), $Cu^{2+}$ (1$\mu_B$), $Cr^{3+}$ (3$\mu_B$), and $Fe^{3+}$ (5$\mu_B$) [93–95]. By considering the cation distribution obtained from XRD analysis, the calculated magnetic moment can be estimated as $n_B^{cal} = 1\ \mu_B$. In terms of Bohr magnetons, the observed magnetic moment can be calculated as follows [92]:

$$n_B^{obs} = \frac{M \times M_s}{5585} \tag{23}$$

The observed $n_B^{obs}$ magnetic moment is calculated using the molecular weight, $M$, and the saturation magnetization value given in emu/g. Using Eq. (23), we find $n_B^{obs} = 0.8\ \mu_B$. This value is close to that obtained for $n_B^{cal}$, indicating a strong correlation between the calculated and observed magnetic properties. This consistency supports the accuracy of the predicted cation distribution in the prepared sample.

### 3.5. Electrical conductivity

In order to investigate the conduction mechanism of the $Cu_{0.4}Mg_{0.4}Co_{0.2}FeCrO_4$ spinel, we have depicted its electrical conductivity ($\sigma$) as a function of frequency and temperature in Fig. 12. Electrical conductivity characterizes a material's ability to conduct electric current when subjected to an applied voltage. It describes the movement of electrons or charge carriers in response to an electric field [96]. In Fig. 12, it can be observed that the $\sigma(T, f)$ curves exhibit consistent variations at different temperatures. At lower frequencies, the $\sigma(T, f)$ curves remain relatively constant. This conductivity behavior, which is consistent with the dc conductivity ($\sigma_{dc}$), indicates the impact of increased activity at grain boundaries. While the increase in $\sigma_{dc}$ values with temperature confirms the semiconductor characteristic of the prepared sample. At higher frequencies, the conductivity shows exponential growth (ac conductivity, $\sigma_{ac}$), which is associated with the conductive behavior of the grains. In many polycrystalline compounds, the $\sigma(T, f)$ curves are often analyzed using Jonscher's law [$\sigma(\omega) = \sigma_{dc} + A \times \omega^s$], where $A$ and $s$ represent temperature-dependent constants and the frequency exponent. However, in our experimental data, this classical equation does not adequately explain the $\sigma(T, f)$ behavior. Therefore, we have employed a modified conduction formula proposed by Jonscher, which incorporates a low-frequency dependence [97]:

$$\sigma = \left[\frac{\sigma_{dc}}{(1+\tau^2\omega^2)}\right] + \left[\frac{(\sigma_{ac}\tau^2\omega^2)}{(1+\tau^2\omega^2)}\right] + A\omega^s \tag{24}$$

where $\tau$, $A$ and $s$ denote the relaxation time, pre-exponential factor, and frequency exponent, respectively. According to Funke's criterion [98], values of $s$ greater than 1 indicate localized hopping between neighboring sites, while $s$ values less than or equal to 1 suggest electron hopping involving translational motion with sudden hopping. The fitting results obtained using Eq. (24) reveal small values for the dc conductivity ($\sigma_{dc}$), indicating significant electrical resistivity in the synthesized sample (Fig. 13a). As a result of this interesting characteristic, our sample may be suitable for microwave devices [99]. Moreover, the $Cu_{0.4}Mg_{0.4}Co_{0.2}FeCrO_4$ ferrite shows much higher electrical resistivity at room temperature compared to some values reported for $Cu_{1-x}Mg_xFe_2O_4$ system [44]. This suggests that the substitution of both $Co^{2+}$ and $Cr^{3+}$ ions in $Cu_{1-x}Mg_xFe_2O_4$ ferrites can enhance their electrical resistivity and their microwave absorption capabilities. In Fig. 13b, it can be observed that the exponent "$s$" decreases with increasing temperature, and all its values are less than unity. This behavior indicates that the conduction process in $Cu_{0.4}Mg_{0.4}Co_{0.2}FeCrO_4$ spinel ferrite follows the Correlated Barrier Hopping model (CBH), where electron hopping involves translational motion with sudden hopping [100]. Furthermore, Fig. 13c depicts the curve of log ($\sigma_{dc} \times T$) as a function of 1000/$T$, which follows this relation [101]:

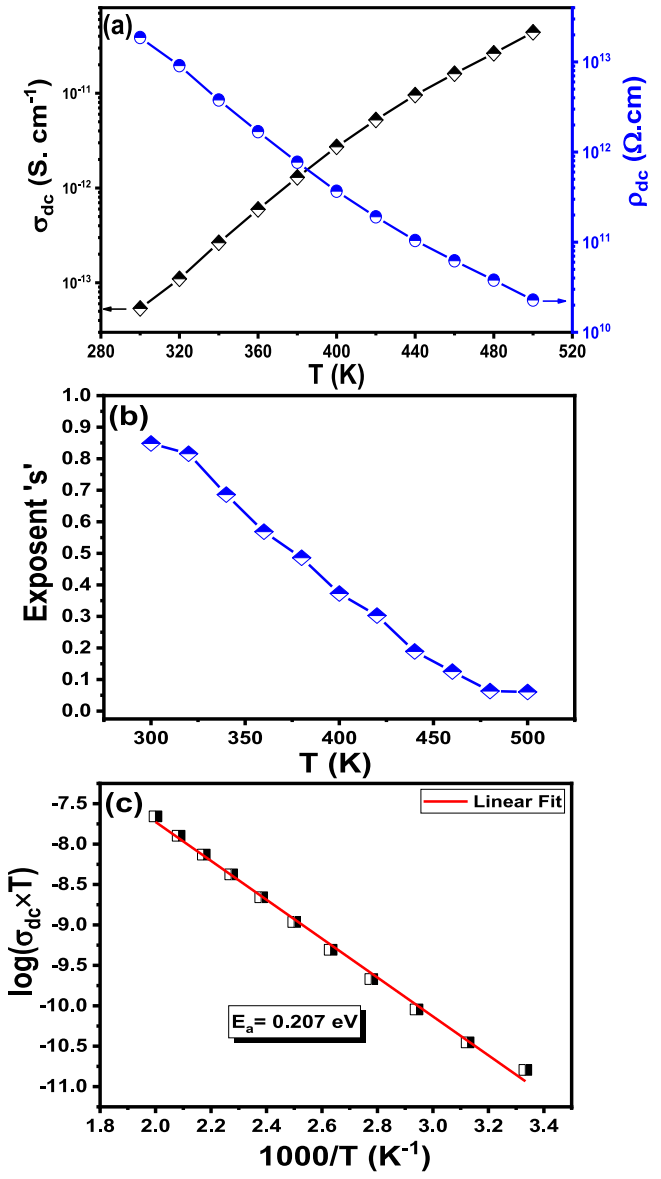


**Fig. 13.** (a) The *dc* conductivity ($\sigma_{dc}$) and the *dc* resistivity ($\rho_{dc}$) versus temperature for $Cu_{0.4}Mg_{0.4}Co_{0.2}FeCrO_4$ spinel ferrite. (b) The exponent (*s*) versus temperature. (c) Plots of log ($\sigma_{dc} \times T$) versus 1000/*T*.

$$\sigma_{dc} = \frac{\sigma_0}{T} exp\left(-\frac{E_a}{k_B T}\right) \quad (25)$$

where $k_B$, $\sigma_0$, and $E_a$ are, respectively, the Boltzmann constant, a pre-exponential factor, and the activation energy. The calculated activation energy ($E_a$) value for $Cu_{0.4}Mg_{0.4}Co_{0.2}FeCrO_4$ spinel ferrite is determined to be 0.21 eV. It is noteworthy that this value is lower compared to the reported $E_a$ values for various compositions of $Cu_{1-x}Mg_xFe_2O_4$ [35,45].

## 4. Conclusion

In conclusion, the structural analysis of $Cu_{0.4}Mg_{0.4}Co_{0.2}FeCrO_4$ spinel ferrite confirms its cubic spinel structure. The band-gap energy ($E_g$) of this sample is determined to be 1.88 eV. The obtained low Urbach energy ($E_u$) of 0.55 eV indicates minimal disorder and defects in the sample. Additionally, the conduction mechanism in the sample follows the CBH model, with an activation energy ($E_a$) of 0.21 eV. The sample demonstrates a lower band gap, coercive field, and activation energy, while exhibiting higher electrical resistivity compared to some $Cu_{1-x}Mg_xFe_2O_4$ compositions. Consequently, substituting both $Co^{2+}$ and $Cr^{3+}$ ions in copper-magnesium ferrites presents an opportunity to enhance their suitability for optoelectronic and electrical applications. In terms of applications, $Cu_{0.4}Mg_{0.4}Co_{0.2}FeCrO_4$ spinel ferrite holds promise in solar cell production due to its light absorption capabilities and photo-catalytic properties. It also serves as a viable candidate for microwave absorption devices and soft magnetic devices.

## CRediT authorship contribution statement

**Mohamed Lamjed Bouazizi:** Writing – review & editing, Writing – original draft, Investigation, Formal analysis, Data curation, Conceptualization. **Sobhi Hcini:** Writing – review & editing, Writing – original draft, Software, Methodology, Data curation, Conceptualization. **Kamel Khirouni:** Visualization, Validation, Resources. **Michel Boudard:** Visualization, Validation, Supervision.

## Declaration of competing interest

The authors declare that they have no known competing financial interests or personal relationships that could have appeared to influence the work reported in this paper.

## Data availability

Data will be made available on request.

## Acknowledgements

This project is sponsored by Prince Sattam bin Abdulaziz University (PSAU) as part of funding for its SDG Roadmap Research Funding Program project number PSAU-2023-SDG.

## References

[1] S. Mu, Q. Liu, P. Kidkhunthod, X. Zhou, W. Wang, Y. Tang, Natl. Sci. Rev. 8 (2021) nwaa178.
[2] Z. Wang, W. Fu, L. Hu, M. Zhao, T. Guo, D. Hrynsphan, S. Tatsiana, J. Chen, Sci. Total Environ. 781 (2021) 146686.
[3] H. Zhang, X. Zhu, Y. Tai, J. Zhou, H. Li, Z. Li, R. Wang, J. Zhang, Y. Zhang, W. Ge, Int. J. Extrem. Manuf. 5 (2023) 032005.
[4] V.P. Sharma, U. Sharma, M. Chattopadhyay, V.N. Shukla, Mater. Today: Proc. 5 (2018) 6376.
[5] S.E. Shirsath, X. Liu, M.H.N. Assadi, A. Younis, Y. Yasukawa, S.K. Karan, J. Zhang, J. Kim, D. Wang, A. Morisako, Y. Yamauchi, S. Li, Nanoscale Horiz 4 (2019) 434.
[6] S.E. Shirsath, X. Liu, Y. Yasukawa, S. Li, A. Morisako, Sci. Rep. 6 (2016) 30074.
[7] S.E. Shirsath, D. Wang, J. Zhang, A. Morisako, S. Li, X. Liu, ACS Appl. Electron. Mater. 2 (2020) 3650.
[8] A. Boutahar, R. Moubah, H. Lemziouika, S. Bahhar, M. Dahbi, M. Ounacer, E. Sebbar, M. Sajieddine, H. Bioud, E.K. Hlil, Indian J. Phys. (2023), https://doi.org/10.1007/s12648-023-03006-1.
[9] S.R. Yousefi, D. Ghanbari, M.S. Niasari, J. Nanostruct. 6 (2016) 77.
[10] P. Mehdizadeh, M. Jamdar, M.A. Mahdi, W.K. Abdulsahib, L.S. Jasim, S. R. Yousefi, M.S. Niasari, Arab. J. Chem. 16 (2023) 104579.
[11] F. Nekkach, H. Lemziouka, A. Boutahar, R. Moubah, M. El Yazidi, E.K. Hlil, Opt. Mater. 147 (2024) 114686.
[12] A. Hiti, F. Nekkach, A. Boutahar, R. Moubah, H. Lemziouka, E.K. Hlil, Opt. Mater. 143 (2023) 114161.
[13] H. Lemziouka, F. Nekkach, A. Boutahar, R. Moubah, L.H. Omari, M. Filali, A. Rjeb, H. Lassri, M. Abid, E.K. Hlil, M. El Yazidi, J. Electron. Mater. 52 (2023) 3420.
[14] Y.N. Li, X.H. Wu, W.W. Wu, et al., J. Supercond. Nov. Magnetism 26 (2013) 2153.
[15] M.G. Naseri, M.K. Halimah, A. Dehzangi, et al., J. Phys. Chem. Solid. 75 (2014) 315.
[16] Y.D. Kolekar, L. Sanchez, E.J. Rubio, et al., Solid State Commun. 184 (2014) 34.
[17] R. Nongjai, S. Khan, K. Asokan, et al., J. Appl. Phys. 112 (2012) 084321.
[18] Z. Gao, B. Xu, M. Ma, et al., Compos. B Eng. 179 (2019) 107417.
[19] J. Wang, B. Wang, A. Feng, et al., J. Alloys Compd. 834 (2020) 155092.
[20] X. Zhou, C. Zhang, M. Zhang, et al., Compos. Part A Appl. Sci. 127 (2019) 105627.
[21] E. Oumezzine, S. Hcini, M. Baazaoui, et al., Powder Technol. 278 (2015) 189.
[22] W. Zhang, A. Sun, X. Zhao, et al., J. Alloys Compd. 816 (2020) 152501.
[23] J. Pei, Z. Wang, Y. Gao, et al., Curr. Appl. Phys. 19 (2019) 440.

[24] S.E. Shirsath, D. Wang, S.S. Jadhav, M.L. Mane, S. Li, Ferrites obtained by sol-gel method, in: L. Klein, M. Aparicio, A. Jitianu (Eds.), Handbook of Sol-Gel Science and Technology, Springer, Cham, 2018, https://doi.org/10.1007/978-3-319-32101-1_125.
[25] N. Mechi, A. Mallah, S. Hcini, et al., J. Supercond. Nov. Magnetism 33 (2020) 1547.
[26] F. Alresheedi, S. Hcini, M.L. Bouazizi, et al., J. Mater. Sci. Mater. Electron. 31 (2020) 8248.
[27] S.A.S. Ebrahimi, S.M. Masoudpanah, J. Magn. Magn Mater. 357 (2014) 77.
[28] N. Kouki, S. Hcini, M. Boudard, et al., RSC Adv. 9 (2019) 1990.
[29] S. Hcini, N. Kouki, A. Omri, et al., J. Magn. Magn Mater. 464 (2018) 91.
[30] C.V. Tran, D.D. La, P.N.T. Hoai, et al., J. Hazard Mater. 420 (2021) 126636.
[31] Y. Zhou, W. Chen, Y. Shen, et al., J. Magn. Magn Mater. 396 (2015) 198.
[32] H.M. Zaki, S.H. Al-Heniti, T.A. Elmosalami, J. Alloys Compd. 633 (2015) 104.
[33] M.A. Ahmed, H.H. Afify, I.K. El Zawawia, A.A. Azab, J. Magn. Magn Mater. 324 (2012) 2199.
[34] T.M. Hammad, S. Kuhn, A.A. Amsha, N.K. Hejazy, R. Hempelmann, J. Supercond. Nov. Magnetism 33 (2020) 3065.
[35] E. Ateia, M.A. Ahmed, R.M. Ghouniem, Solid State Sci. 31 (2014) 99.
[36] Y. Piña-Pérez, F. Tzompantzi-Morales, R. Pérez-Hernández, et al., Fuel 198 (2017) 11.
[37] X. Zhu, W. Yuan, M. Lang, et al., Fuel 252 (2019) 148.
[38] Q. Li, B. Guo, J. Yu, et al., J. Am. Chem. Soc. 133 (2011) 10878.
[39] D.D. La, C.V. Tran, N.T.T. Hoang, et al., Fuel 281 (2020) 118655.
[40] C. Kumari, H.K. Dubey, F. Naaz, et al., Phase Transitions 93 (2020) 207.
[41] A.A. El-Fadl, A.M. Hassan, M.A. Kassem, Results Phys. 28 (2021) 104622.
[42] J.S. Ghodake, R.C. Kambaleb, S.V. Salvi, S.R. Sawant, S.S. Suryavanshi, J. Alloys Compd. 486 (2009) 830.
[43] M.V. Chaudhari, S.E. Shirsath, A.B. Kadam, R.H. Kadam, S.B. Shelke, D.R. Mane, J. Alloys Compd. 552 (2013) 443.
[44] S. Akhter, D.P. Paul, D. Saha, S.M. Hoque, M.A. Hakim, J. Sci. Res. 6 (2014) 205.
[45] S. Kainuma, Jpn. J. Appl. Phys. 15 (1976) 1079.
[46] L. Guo, X. Shen, X. Meng, et al., J. Alloys Compd. 490 (2010) 301.
[47] S.B. Somvanshi, M.V. Khedkar, P.B. Kharat, et al., Ceram. Int. 46 (2020) 8640.
[48] T. Roisnel, J. Rodriguez-Carvajal, Computer Program FULLPROF, LLB-LCSIM, 2003.
[49] L. Wang, M. Lu, Y. Liu, et al., Ceram. Int. 41 (2015) 4176.
[50] Q. Lin, Y. He, J. Lin, et al., J. Magn. Magn Mater. 469 (2019) 89.
[51] N. Kouki, S. Hcini, Raldowas, et al., J. Supercond. Nov. Magnetism 32 (2019) 2209.
[52] F. Hcini, S. Hcini, B. Alzahrani, et al., Appl. Phys. A 126 (2020) 362.
[53] G. Kumar, R.K. Kotnala, J. Shah, V. Kumar, A. Kumar, P. Dhiman, M. Singh, Phys. Chem. Chem. Phys. 19 (2017) 16669.
[54] I. Khishigdemberel, E. Uyanga, H. Hirazawa, et al., Physica B 544 (2018) 73.
[55] J. Li, X. Wang, K. Song, et al., IEEE Trans. Magn. 51 (2015) 1.
[56] S. AbuBakar, N. Soltani, W.M.M. Yunus, et al., Solid State Commun. 192 (2014) 15.
[57] E. AlArfaj, S. Hcini, A. Mallah, et al., J. Supercond. Nov. Magnetism 31 (2018) 4107.
[58] K. Souifi, O. Rejaiba, O. Amorri, et al., J. Inorg. Organomet. Polym. 32 (2022) 4515.
[59] G. Raddaoui, O. Rejaiba, M. Nasri, et al., J. Mater. Sci. Mater. Electron. 33 (2022) 21890.
[60] J. Wang, C. Zhang, H. Liu, et al., Nat. Commun. 10 (2019) 129.
[61] O. Rejaiba, K. Khirouni, M.H. Dhaou, et al., Opt. Quant. Electron. 54 (2022) 315.
[62] K. Gagandeep, B.S. Lark Singh, et al., Nucl. Sci. Eng. 134 (2000) 208.
[63] S.M.H. Qaid, B.A. Al-Asbahi, H.M. Ghaithan, et al., J. Colloid Interface Sci. 563 (2020) 426.
[64] A. Fujishima, X. Zhang, D.A. Tryk, Surf. Sci. Rep. 63 (2008) 515.
[65] J. Xie, H. Wang, M. Duan, et al., Appl. Surf. Sci. 257 (2011) 6358.
[66] N.R. Dhineshbabu, V. Rajendran, N. Nithyavathy, et al., Appl. Nanosci. 6 (2016) 933.
[67] F. Hcini, S. Hcin, M.M. Almoneef, et al., J. Mol. Struct. 1243 (2021) 130769.
[68] S.A. Moyez, S. Roy, J. Nanoparticle Res. 20 (2017) 5.
[69] A. Bougrine, A. El Hichou, M. Addou, et al., Mater. Chem. Phys. 80 (2003) 438.
[70] A.M. Mansour, M. Nasr, H.A. Saleh, et al., Appl. Phys. A 125 (2019) 625.
[71] S. Husain, A.O.A. Keelani, W. Khan, Nano-Struct. Nano-Objects. 15 (2018) 17.
[72] A. Ben Jazia Kharrat, K. Kahouli, S. Chaabouni, Bull. Mater. Sci. 43 (2020) 275.
[73] A.M. El Nahrawy, B.A. Hemdan, A.M. Mansour, et al., Silicon 14 (2022) 6645.
[74] B.A. Hemdan, A.M. El Nahrawy, A.F.M. Mansour, et al., Environ. Sci. Pollut. Res. 26 (2019) 9508.
[75] F. Hcini, S. Hcini, M.A. Wederni, et al., Physica B 624 (2022) 413439.
[76] A.M. Mansour, B.A. Hemdan, A. Elzwawy, et al., Sci. Rep. 12 (2022) 9855.
[77] S.H. Wemple, M. Didomenico, Phys. Rev. B 3 (1971) 1338.
[78] N. Tounsi, A. Barhoumi, F.C. Akkari, et al., Vacuum 121 (2015) 9.
[79] H. Yokokawa, N. Sakai, T. Kawada, et al., Solid State Ionics 52 (1992) 43.
[80] M. Fox, Optical Properties of Solids, 2th ed., Oxford University Press, New York, 2010.
[81] R. Mguedla, A. Ben Jazia Kharrat, N. Moutia, et al., J. Alloys Compd. 836 (2020) 155186.
[82] E.A. Davis, N.F. Mott, Philos. Mag. A 22 (1970) 903.
[83] Z. Raddaoui, B. Smiri, A. Maaoui, et al., RSC Adv. 8 (2018) 27870.
[84] Y. Feng, S. Lin, S. Huang, et al., J. Appl. Phys. 117 (2015) 125701.
[85] S.R. Chalana, V. Ganesan, V.P.M. Pillai, AIP Adv. 5 (2015) 107207.
[86] G.V. Makhnovets, G.L. Myronchuk, L.V. Piskach, et al., J. Phys. Opt. 19 (2018) 49.
[87] K. Kahouli, A. Ben Jazia Kharrat, S. Chaabouni, Indian J. Phys. 95 (2021) 2797.
[88] H. Shokrollahi, K. Janghorban, J. Mater. Process. Technol. 189 (2007) 1.
[89] P.K. Chakrabarti, B.K. Nath, S. Brahma, S. Das, D. Das, M. Ammar, et al., Solid State Commun. 144 (2007) 305.
[90] S. Modak, M. Ammar, F. Mazaleyrat, S. Das, P.K. Chakrabarti, J. Alloys Compd. 473 (2009) 15.
[91] L. Néel, Science 174 (1971) 985.
[92] S. Torkian, A. Ghasemi, R.S. Razavi, Ceram. Int. 43 (2017) 6987.
[93] G. Satyanarayana, G.N. Rao, K.V. Babu, G.V.S. Kumar, G.D. Reddy, J. Kor. Phys. Soc. 74 (2019) 684.
[94] M. Satalkar, S.N. Kane, J. Phys. Conf. Ser. 755 (2016) 012050.
[95] Y. Han, A. Sun, X. Pan, W. Zhang, X. Zhao, J. Supercond. Nov. Magnetism 32 (2019) 3823.
[96] C. Kittel, Introduction to Solid State Physics, eighth ed., John Wiley & Sons, 2004.
[97] M. Sassi, A. Oueslati, M. Gargouri, Appl. Phys. A 119 (2015) 763.
[98] K. Funke, Prog. Solid State Chem. 22 (1993) 111.
[99] I. Sadiq, S. Naseem, M.N. Ashiq, M.A. Khan, S. Niaz, M.U. Rana, Prog. Nat. Sci. Mater. Int. 25 (2015) 419.
[100] M.B. Bechir, K. Karoui, M. Tabellout, K. Guidara, A.B. Rhaiem, J. Appl. Phys. 115 (2014) 203712.
[101] F. Hcini, S. Hcini, B. Alzahrani, S. Zemni, M.L. Bouazizi, J. Mater. Sci. Mater. Electron. 31 (2020) 14986.